

Passive acoustic determination of spectral wave breaking dissipation



Xiaochen Zou,^a Alexander V. Babanin,^b Eric Werner Schulz,^c Richard Manasseh,^d
Changlong Guan.^a

^a *College of Oceanic and Atmospheric Sciences, Ocean University of China, Qingdao, China*

^b *Department of Infrastructure Engineering, University of Melbourne, Melbourne, Victoria, Australia*

^c *Bureau of Meteorology, Australia*

^d *Swinburne University of Technology, Australia*

Corresponding author: Xiaochen Zou, zouxc1122@qq.com

ABSTRACT

When a wave breaks, it produces bubbles whose sizes depend on the breaking severity. This paper attempts to estimate wave breaking dissipation through a passive acoustic method. Initially, regular waves were forced to break in a flume. The breaking energy loss (severity) and the underwater acoustic noise were recorded. Two kinds of thresholds, in terms of sound wave amplitude and the ratio of sound wave height to period, respectively, were used together to identify the sound waves generated by newly formed bubbles. The frequencies of these sound waves are connected with the bubble sizes. Thus, a relationship between the mean bubble radius and the breaking severity was established and found to be linear. This laboratory relationship was then applied to Lake George data to study the breaking dissipation rate across the spectrum. An average acoustic spectral density threshold was proposed to identify breaking events from acoustic records in the field. The sound waves associated with bubble formation were selected by means of the same two kinds of threshold as used in the laboratory. Thus, the mean bubble radius of each breaking event was obtained and translated into the breaking severity. The values of experimental dissipation were compared with previous relevant results obtained through different methods as well as the wave breaking dissipation source terms ST6 (WAVEWATCH-III model) and are in good agreement with both of them.

1. Introduction

The breaking of wind-generated wave is one of the most prominent phenomena at the ocean surface, playing a primary role in the air-sea exchange of momentum, mass and heat and is of significant importance for maritime and coastal engineering. Being the most effective process of energy dissipation, wave breaking is a critical mechanism involved in the wave forecasting models. Although great effort has been put into it, the understanding of wave breaking is still quite limited. As a result, the spectral dissipation functions employed in wave models have to rely on hypotheses and speculations.

Research on wave breaking has long been a challenge. Hydrodynamic theory for irrotational flow becomes invalid once a wave is breaking. Numerical modeling has to solve the basic equations for two-phase turbulent flows, which makes it rather computationally demanding. Until now we had to rely on laboratory and field measurements. However, due to its intermittency and randomness, the experimental measurement of wave breaking is very

difficult. Visual observation used to be the only reliable means of breaking detection in earlier times (e.g. Munk 1947; Weissman et al. 1984; among many others). Although most of the wave records do have breakers in them, usually those go undetected. Lately, methods based on wavelet analysis were developed to distinguish breaking waves from those non-breaking in such time series of surface elevations (Liu and Babanin, 2004, Liberzon et al. 2019). In recent years, more technologies have been employed to identify breaking events, based on acoustic, optical, conductivity and other properties of breakers which differentiate them from the more homogeneous background. With the help of wave probes, PIV (Particle Image Velocimetry) and other measuring instruments, the geometry and hydrodynamics of breaking waves were also investigated.

Although many new techniques are now available, most of them are intent on measuring breaking probability rather than breaking severity. Breaking severity is defined as the amount of energy density lost in an individual breaking event, $E_b - E_a$, where E_b and E_a represent the wave energy density before and after breaking, respectively. Its nondimensional counterpart is the severity coefficient s which is defined as the fraction of wave energy lost in breaking:

$$s = \frac{E_b - E_a}{E_b}. \quad (1)$$

There are some estimations of s in terms of wave height. Hwang et al. (1989) calculated the ratio of wave height loss of laboratory breaking wind waves and found it to be about 30%, which is equivalent to $s \sim 50\%$ (Babanin 2011). Laboratory experiments on unsteady deep-water breaking by Rapp and Melville (1990) yielded a quite different value, $s \sim 10\%$. Babanin (2011) estimated s of the Black Sea waves and got $s \sim 99\%$. These results of s varied greatly. Babanin (2011) argued that the severity coefficient depends on breaking mechanism and its estimation in terms of wave height is inaccurate. For more details about these discussions the reader is referred to Babanin (2011).

The observations dealing with breaking spectral dissipation are very few and the outcomes are quite diverse. By means of frequency dispersion, Rapp and Melville (1990), Kway et al. (1998) and Meza et al. (2000) found that the major breaking dissipation occurs at high frequency, whereas the spectral peak remains unchanged. Pierson et al. (1992), stimulating breaking through amplitude dispersion, obtained an opposite conclusion that the

most severe dissipation occurs around the spectral peak, while some components of the spectrum (of scales both below and above the scale of the breaker) actually gain energy. Young and Babanin (2006, here in after YB06) analyzed a wave record measured at Lake George of which about half of the dominant waves broke. Their results show about 40% energy loss in the peak region of the wave spectrum (Babanin 2011). Moreover, they emphasized that the dominant breaking not only induces energy loss to itself, but also to high-frequency waves. That is the so-called cumulative effect. More measurements are needed to understand the spectral dissipation. We should note that most of the wave-breaking and whitecap-dissipation research, particularly in laboratory, presumes unidirectional waves, whereas real wind-forced waves always have a directional distribution of their energy, in addition to frequency spectrum, and this modifies both the breaking probability (Babanin et al. 2010) and breaking severity (YB06).

The direct way to obtain breaking severity is to measure the wave energy difference immediately before and immediately after a breaking event. This is impossible in the open field due to the randomness of wave-breaking occurrence. Until now such measurements have only been conducted in the laboratory, where, through various artificial means, the location of the breaking event can be accurately controlled between two wave probes (e.g. Rapp and Melville 1990; Meza et al. 2000; Manasseh et al. 2006). These experiments were usually intended to find the relationship between wave energy loss and the pre-breaking wave characteristics (such as wave height, frequency and/or wavelength). These observations are very helpful in understanding breaking dissipation. However, as has been mentioned before, the energy dissipation depends on the way the waves are driven to break, which may be different in the laboratory and in natural circumstances, thus it is doubtful whether these relationships fit for the open field.

Manasseh et al. (2006, here in after M06) developed a bubble-detection technique, which is promising in breaking dissipation measurement in the open field. They used a hydrophone to record the ambient noise, from which wave breaking events can be identified and their severities can be derived. Since the sound attenuation in water is relatively low, the hydrophones can be installed underwater to avoid destruction from hurricanes (Wilson and Makris 2008). Moreover, the hydrophone is battery-powered and of low power consumption which makes it capable for long-term observations. The ambient noise recorded by the hydrophone may come from many sources, such as precipitation, biological sources and wave

breaking. Once the latter occurs, it will become the primary one (Kerman 1992; Bass and Hay 1997; among many others). Wind and wave effects are most prominent in the frequency band of 0.1-10 kHz. Both the laboratory experiment of Loewen and Melville (1991) and the field measurement of Felizardo and Melville (1995) showed a good correlation of the acoustic noise level in this band with wave breaking dissipation. Furthermore, Bass and Hay (1997) and Babanin et al. (2001) demonstrated that wave breaking results in evident enhancement in the sound spectrum above 0.5 kHz. Theoretical work (e.g. Medwin 1989) suggested that the bubble-formation process dominates the frequency range 0.5-10 kHz. The remaining part of the band, 0.1-0.5 kHz, is likely to be produced by bubble clouds, rather than individual bubbles (e.g. Prosperetti 1988; Lu et al. 1990; Tkalich and Chan 2002).

It has been well known since the time of Rayleigh (1917) that once a bubble is formed, its volume oscillates with a natural frequency depending on its size. The simple harmonic solution of the Rayleigh-Plesset equation describing bubble acoustic oscillation gives

$$\omega_0 = \sqrt{\frac{3\gamma p_0}{\rho}} \frac{1}{R_0} \quad (2)$$

(Minnaert 1933), where ω_0 is the radian frequency, γ is the ratio of specific heats of the gas, p_0 is the absolute liquid pressure, ρ is the liquid density and R_0 is the equivalent spherical radius of the bubble. The oscillating bubble emits sound and this ringing may last about 10-20 cycles. Both amplitude and frequency of this ringing keep dropping while the amplitude of the earliest cycle is the highest and its frequency is closest to the theoretical natural frequency given by Eq. (2) (Manasseh 1997; Chen et al. 2003; Roshid and Manasseh 2020). Therefore, once wave breaking occurs, the accompanied bubble formation would produce prominent and sharp acoustic pulses, from which not only the breaking event can be recognized, but also the mean bubble radius can be drawn. The latter is expected to increase with breaking severity. Based on these theories, M06 proposed to measure breaking severity through detecting bubbles formed during the breaking process. They applied this method to Lake George experiment data and also conducted laboratory experiments. In their work, the sound waves emitted by individual freshly formed bubbles were captured when the instantaneous sound pressure exceeded a sound pressure threshold. The frequencies of these sound waves were measured and translated into bubble radii according to Eq. (2). Although preliminary, the laboratory results show clearly that the bubble size increases with the breaking severity

estimated in terms of wave heights, and the mean bubble sizes demonstrate a good positive correlation with wind speeds in Lake George.

In this paper, more laboratory experiments are carried out to further investigate the relationship between bubble size and breaking severity, and an empirical relationship between the two is established. This relationship is then applied to the Lake George experiment data to study the spectral dissipation rate in wave field. The paper is organized as follows. In section 2, the laboratory experiments are described and an empirical relationship is established. In section 3, the field experimental setup is outlined and the records are analyzed to calculate the mean bubble radius of each breaking event. In section 4, the spectral dissipation rates in Lake George are calculated and compared with the results of YB06 and the ST6 source term. Conclusions are summarized in section 5.

2. Laboratory experiment and parameterization

a. Laboratory experimental setup

To investigate the relationship between mean bubble radius and breaking severity, laboratory experiments were carried out in a flume at the University of Adelaide. The flume is 1.215 m wide with water depth of 225 ± 5 mm above a sandy bottom. Regular waves of various heights and frequencies (as listed in Table 1) were generated mechanically. In order to trigger wave breaking at a designated position, a vertical board of 45 mm wide and 150 mm high was placed 10 m downstream of the wave maker with its top 50 mm below the mean water level. Every wave was forced to break over this barrier. Two capacitance probes measured the instantaneous water elevations, 640 mm upstream of the board and 560 mm downstream of the board, with sampling rate of 19 Hz. Right under the bubble formation zone, a hydrophone was installed 60 mm downstream of the board with its tip 55 mm below the mean water level. The hydrophone worked at sampling rate of 19 kHz and was calibrated so that 1 V output represented 100 Pa sound pressure. The time length of each record is 60 s. The raw acoustic signals were detrended and high-passed at 0.5 kHz cut-off frequency before further analysis in section 2b. Typical time series of surface elevation and high-pass-filtered hydrophone output are shown in Fig. 1.

No.	H (cm)	f (Hz)
-----	----------	----------

1	4.0	1.0
2	4.2	0.9
3	5.4	0.9
4	5.4	0.9
5	5.6	0.9
6	6.9	0.9
7	7.7	1.0
8	8.6	0.8
9	8.7	1.0
10	8.8	0.8
11	10.0	1.0
12	10.0	1.0

Table 1. Summary of mechanically generated wave records. H , wave height; f , wave frequency.

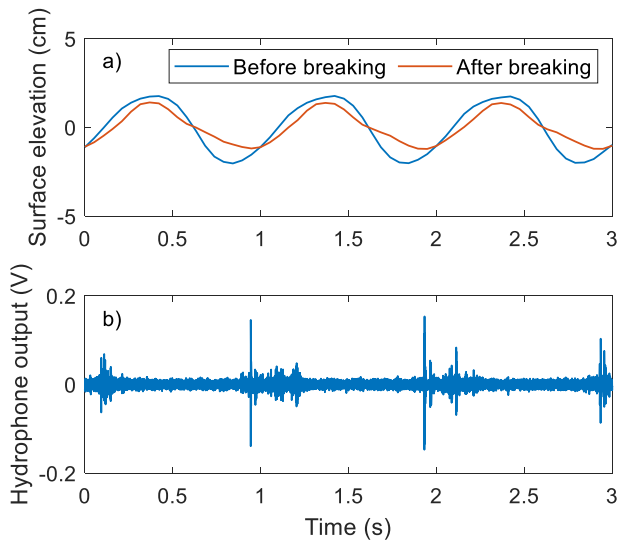


Fig. 1. A segment of time series of (a) surface elevation and (b) high-pass-filtered hydrophone output from record 1 of Table 1.

b. Bubble radius calculation and the dependence of bubble radius on breaking severity

As shown in Fig. 1, each breaking event generates a prominent pulse group over the nearly stationary background noise. Since the background noise level is almost the same in all acoustic records, the high pulse groups can be differentiated from the background noise by a constant sound amplitude threshold T_A . The value of T_A is set to be 0.015 V which is slightly higher than the upper envelope of background noise.

Zooming in on the high pulse groups, one can find more information. Fig. 2(a) shows a typical noise segment within a high pulse group. For the convenience of the following analysis, we define an individual sound wave as the signal between two adjacent zero-upcrossings, and its temporal steepness S_t as the ratio of its height H_{sw} to its period T_{sw} ,

$$S_t = \frac{H_{sw}}{T_{sw}}. \quad (3)$$

In Fig. 2(a), the sound waves with amplitudes exceeding T_A are divided into two types according to their S_t and are plotted in red ($S_t \geq 50$) and yellow ($S_t < 50$) separately. The red sound waves exhibit sharp waveforms, most of which are likely being emitted by newly-formed bubbles. In contrast, the yellow ones have long zero-upcrossing periods and appear to be dominated by background noise. As shown in Fig. 2(b), the temporal steepness S_t of the red sound waves are well above those of the yellow ones. This implies that the latter can be excluded by an appropriate temporal steepness threshold T_s . After visually examining the first 2 seconds of each acoustic record of Table 1, the value of T_s is determined to be 50 V s^{-1} which works well in all cases.

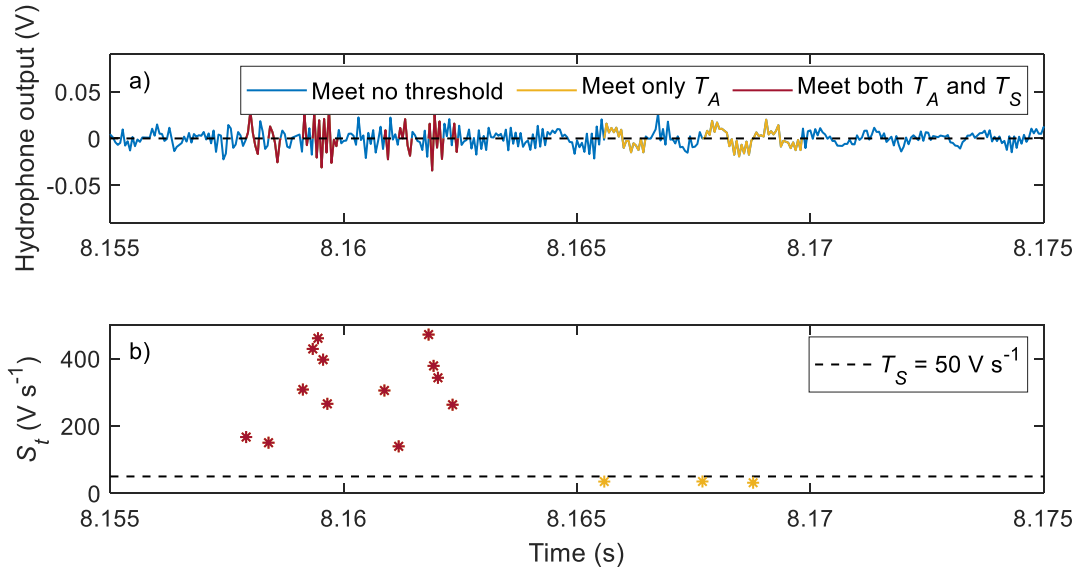


Fig. 2. Detailed inspection of the breaking signature in hydrophone output. (a) Time series of hydrophone output. The sound waves are selected by the amplitude threshold T_A (yellow) and further by the temporal steepness threshold T_S (red). (b) The temporal steepness S_t (Eq. (3)) of the sound waves. The temporal steepness threshold $T_S = 50 \text{ V s}^{-1}$ is shown as the dashed line. The acoustic segment is taken from record 1 of Table 1.

It should be noted that $T_S = 50 \text{ V s}^{-1}$ is chosen to exclude only the sound waves obviously dominated by background noise. This threshold value can be taken as a lower bound. In contrast to the sharp sound waves emitted by fresh bubbles (i.e. true selections), there must be some sound waves slightly above T_S but not emitted by the bubbles (i.e. false selections). Considering that the frequency difference between the sound waves within one pulse is usually much smaller than the difference between the true and false selections, the inclusion of multiple sound waves in one pulse can reduce the bias caused by false selections. In light of this, all the sound waves meet both T_A and T_S criteria are used to estimate the mean bubble radius R of each record. Their periods are read and translated into bubble radii according to Eq. (2), then averaged to obtain R .

The size distributions of individual bubbles thus obtained are shown in Fig. 3. Three records are selected to represent the weak, medium and strong breakers in the laboratory experiment. One can see that the bubble size distribution shows a peak which shifts to a larger radius and becomes more concentrated as breaking becomes more severe. For all records, the probability density of bubble radius decreases with increasing frequency at high

frequencies, and is quite low when approaching the Nyquist frequency of 9.5 kHz. Therefore, the limitation of the sampling rate would not induce significant bias or aliasing.

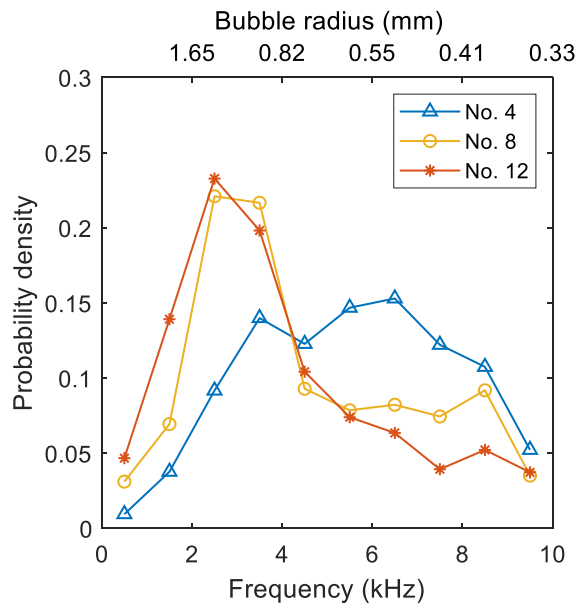


Fig. 3. Size distributions of individual bubbles measured in laboratory. The blue, yellow and red lines correspond to record No. 4, 8 and 12 of Table 1, respectively.

It is worth noting that, the acoustically detected bubble size distributions shown in Fig. 3 are different from typical optically obtained results (e.g. Deane and Stokes 2002, here in after DS02) which are proportional to a negative power of the radius. The discrepancies are primarily due to the different bubble collections observed by the two techniques. While DS02 measured all the visible bubbles in the photographs, the present study detects only the freshly formed individual bubbles with sound pulses higher than background noise level. Compared to DS02, the acoustic statistics do not account for the bubbles inside the bubble clouds (with sound frequency typically below 0.5 kHz) and the bubbles emitting weak sound pulses. Besides that, DS02 measured the mean bubble size spectrum from photographs taken at a variety of times across the whole acoustically active phase, during which the large bubbles are passing through a fragmentation cascade. These ephemeral bubbles have short lives, and their numbers are underestimated by the time averaging, but contribute to the acoustic record (Deane and Stokes 2008). The above facts may result in significant differences in bubble size distribution.

In this paper, the breaking severity normalized by the water density ρ_w and the gravitational acceleration g is employed to represent the breaking severity, denoted by ΔE , and is calculated according to

$$\Delta E = \frac{\int_0^T (\zeta_u^2 - \zeta_d^2) dt}{T} \quad (4)$$

where $T = 60$ s is the time length of a wave record, ζ_u and ζ_d are the surface elevations measured by the two wave probes upstream and downstream of the barrier. In Fig. 4(a), ΔE versus R is plotted as circles for the laboratory records of Table 1. The results show a nearly linear relationship with more severe breaking generating larger bubbles. The least-squares fitting yields

$$\Delta E = 0.63(R - 6.87 \cdot 10^{-4}) \quad (5)$$

where all variables are in SI units. Earlier results (M06) showed that the rate of bubble detection as well as the mean bubble size increased with wind speed, thus it seems likely that there are more large bubbles, i.e. the bubble-size spectrum shifts for more energetic wave-breaking events. In agreement with M06, the acoustically detected size distributions of individual bubbles (Fig. 3) also demonstrate the increase of large bubble percentage as breaking becomes more severe, and consequently the mean bubble radius R increase with breaking severity ΔE .

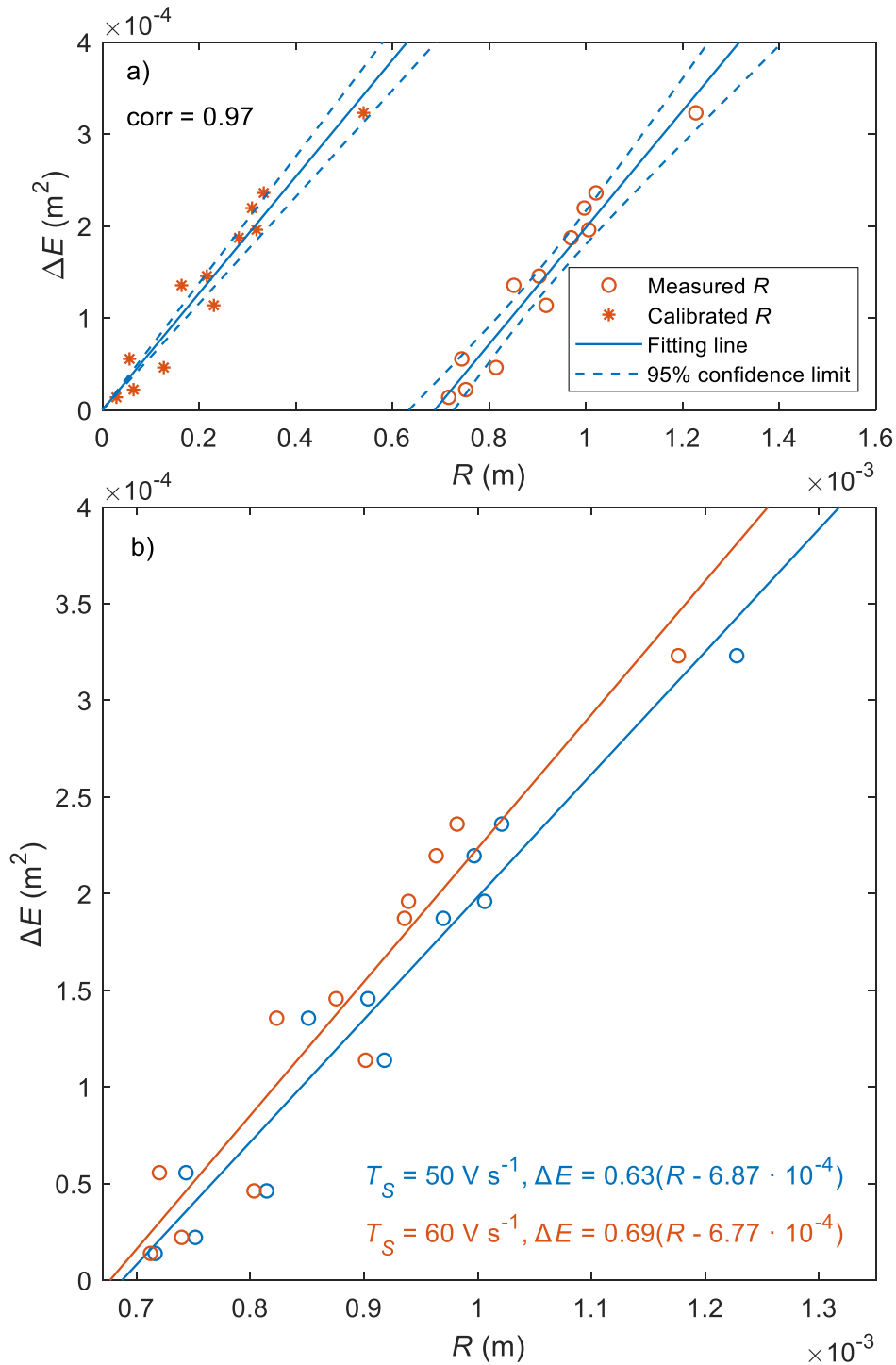


Fig. 4. (a) Laboratory breaking severity ΔE vs measured bubble radius R (o) and its calibrated counterpart (*). The right and left fitting lines correspond to Eq. (5) and Eq. (6), respectively. The 95% confidence limits are shown with dashed lines. (b) Sensitivity test of Eq. (5) for the temporal steepness threshold T_S . The blue and red colours correspond to $T_S = 50 \text{ V s}^{-1}$ and $T_S = 60 \text{ V s}^{-1}$, respectively.

We should note that the estimation of mean bubble radii relies on the values of the two thresholds, T_A and T_S . Since T_A is set slightly higher than the upper envelope of nearly stationary background noise, its magnitude could be regarded as objective. The value of T_S , however, is set as a lower bound. To examine the sensitivity of Eq. (5) to T_S , the results with $T_S = 50 \text{ V s}^{-1}$ and $T_S = 60 \text{ V s}^{-1}$ are compared in Fig. 4(b). It can be seen that the fitting parameters with $T_S = 60 \text{ V s}^{-1}$ vary marginally from the ones with $T_S = 50 \text{ V s}^{-1}$, indicating that the relationship is not very sensitive to the value of T_S .

There is an unexpected offset in Eq. (5) which is physically unreasonable, since ΔE is expected to become zero at $R = 0$. This offset can be regarded as a systematic error coming from the bubble detection method used here. A limitation of acoustic detection is that those weak pulses (also emitted by individual bubbles) mixed up with background noise could not be identified. While Eq. (2) provides an immediate link between bubble size and frequency, albeit a complex link when multiple bubbles are present (Roshid and Manasseh 2020), it has long been recognized that the spectra of complex bubbly flows will be biased towards larger bubbles, since it is thought likely that larger bubbles emit higher-amplitude sounds. Attempts to account for this have hitherto required assumptions on the relative magnitude of the perturbation exciting the bubble sound emission (Pandit et al. 1992; Chanson and Manasseh 2003). One model predicting sound amplitude from bubble size, for a specific formation mechanism, that of Deane and Stokes (2008), does not predict a monotonic increase of amplitude with bubble size, whereas recent experiments (Nelli et al. 2022) do demonstrate a monotonic increase with bubble size. If smaller bubbles do emit weaker sound, then very small bubbles cannot be detected. Furthermore, usually multiple sound waves within a pulse are selected; thus the louder the pulse, the more sound waves might be selected. Consequently, the apparent mean bubble radius R may be biased towards larger sizes. Furthermore, T_S is chosen as a lower bound can also induce some enlargement. In consideration of these overestimations and the physical rationality, we take the offset in Eq. (5) as a systematic error and approximate the actual R as the measured value minus the offset $6.87 \cdot 10^{-4}$ m. Therefore, the relationship between ΔE and R is calibrated to be

$$\Delta E = 0.63R. \quad (6)$$

It is worth pointing out that there should be a limit of breaking severity beyond which Eq. (6) is inapplicable. As breakers become more energetic, ever-larger voids of air should become entrained. Evidently, large plunging breakers do transiently enclose very large air cavities (e.g. Fig. 10.1 in Manasseh 2021), tens of cm or even meters in size. Some cavities are never completely disconnected from the atmosphere, while others immediately break up into smaller voids that in turn fragment into bubbles. It is not clear if the air in the large cavities is compressed consistently, creating sound, and, moreover, the surrounding water is so full of other large cavities that the concept of an infinite liquid surrounding a single small bubble that underpins Minnaert's equation is no longer valid. Thus, we should expect a limit to the relation between breaker energy loss and acoustically-detectable bubble size. It seems the present experiments (as well as the Lake George observations in Section 3 and 4) did not involve breakers energetic enough for this limit to be reached.

c. Nondimensionalization of laboratory relationship

Eq. (6) is dimensional and therefore the dependence is not generally applicable. Here we try to nondimensionalize it through dimensional analysis. For this aim, we infer the factors controlling R from related physics as well as the observations. Physically, R depends directly on breaking strength rather than the pre-breaking wave characteristics (wave height and wavelength). Although the breaking strength is closely related to pre-breaking wave characteristics, it may also depend on breaking mechanism. Therefore, ΔE is a better choice than pre-breaking wave characteristics to represent the dependence of R on breaking strength. In Fig. 4(a), the datapoints corresponding to various pre-breaking wave heights and wavelengths fall quite close to the fitting line. Similar results were found by M06. In their research, waves with frequency 0.75 Hz and various amplitudes were generated and forced to break. They estimated the breaking severity in terms of the difference in squared wave height of monochromatic waves before and after breaking, $H_b^2 - H_a^2$. In their Fig. 6, the increase of R with $H_b^2 - H_a^2$ is also approximately linear. These experiments demonstrate that R is well associated with breaking severity while the influence of pre-breaking wave characteristics on this relationship is not evident. Furthermore, the gravity plays a key role in the process of wave breaking and the bubble production involves the air and water two-phase flow. Since the bubble size range inferred includes bubbles below millimeter order, the surface tension is also important. For these reasons, the gravitational acceleration g , the water density ρ_w , the air density ρ_a as well as the surface tension coefficient σ shall all be

introduced into the nondimensional dependence of R as a function of breaking severity ΔE .

In light of these considerations, we assume

$$R = R(\Delta E, \rho_w, \rho_a, g, \sigma). \quad (7)$$

Following the Pi-Theorem (Buckingham 1914) we define three dimensionless quantities as

$$\tilde{R} = \frac{R}{\sqrt{\sigma/(\rho_w g)}}, \quad (8)$$

$$\Delta\tilde{E} = \frac{\Delta E}{\sigma/(\rho_w g)}, \quad (9)$$

and

$$\tilde{\rho} = \frac{\rho_a}{\rho_w}, \quad (10)$$

and obtain

$$\tilde{R} = \tilde{R}(\Delta\tilde{E}, \tilde{\rho}). \quad (11)$$

Since, from the results of the previous section, R depends linearly on ΔE , and moreover,

$R = 0$ when $\Delta E = 0$, the function in Eq. (11) shall be

$$\tilde{R} = f(\tilde{\rho})\Delta\tilde{E}. \quad (12)$$

Following the Pi-Theorem,

$$\tilde{R} = a\tilde{\rho}\Delta\tilde{E} \quad (13)$$

where a is a measurement constant to be found experimentally. Based on the laboratory measurements, the least-squares fitting yields

$$\tilde{R} = 3.56\tilde{\rho}\Delta\tilde{E} \quad (14)$$

which is shown in Fig. 5.

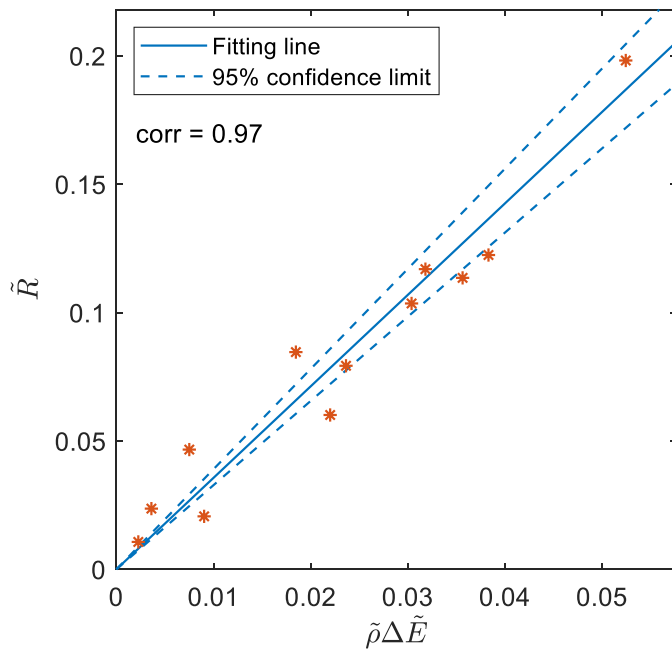


Fig. 5. Nondimensional relationship between \tilde{R} and $\tilde{\rho}\Delta\tilde{E}$. The best fit line (Eq. (14)) and 95% confidence limit are also shown.

3. Field experiment and data processing

a. Field experimental setup

The field data used in this study comes from the experiments at Lake George, Australia during 1997-2000. The experiments aimed at studying the source and sink functions of fetch-limited wind waves in a finite-depth environment. Full details of the experiments are given in Young et al. (2005). Here only the relevant measurements are briefly described.

The measurements were carried out on a 10m-long bridge on the side of an instrumented platform, which is located 50 m from the eastern shore of Lake George, beyond the surf zone. The bed form of Lake George is extremely flat. The observation area was exposed to the prevailing westerly wind and the corresponding longest wave fetch. The water surface elevation about half-way along the bridge was measured by an array of capacitance gauges with sampling rate of 25 Hz. During the experimental period, the water depth at measurement point ranged between 0.84 m and 1.10 m. A hydrophone was located on the bottom directly beneath the wave probes to synchronously record the noise generated by breaking waves, with its sensing head 20 cm above the bottom. The hydrophone's sampling rate was 8 kHz. A

vertical array of six cup anemometers and two wind vanes were installed on anemometer masts to measure the boundary layer wind profile.

The acoustic signal was saved on the audio channel of video tape at a fixed gain. However, the present analysis was not anticipated at the time of the experiment and the actual value of this gain cannot be confirmed now. Following M06, the signal levels are reported in this paper in Volts, to emphasize that the precise magnitudes of the acoustic thresholds relevant to signal levels calculated in section 3c may be specific to the present data.

As we have done with the laboratory analysis, the raw field signals were also detrended and high-passed at 0.5 kHz cut-off frequency. Table 2 shows the wind-wave parameters for all 26 records. Each record lasted 20 minutes. The quality of acoustic data is examined at first. Out of the 26 records, No.1 and No.2 were found abnormal which contain some extremely high pulses. Since there are very few breaking events in these two records, these pulses can bring significant errors to bubble detection. Hence, only the other 24 records are used here.

No.	Run	f_p (Hz)	H_s (m)	U_{10} (m s ⁻¹)	b_T
1	311501.oc7	0.48	0.21	11.0	0.016
2	311615.oc7	0.48	0.17	8.5	0.007
3	311638.oc7	0.49	0.17	9.4	0.005
4	311757.oc7	0.42	0.35	17.1	0.375
5	311823.oc7	0.36	0.45	19.8	0.600
6	311845.oc7	0.33	0.40	15.0	0.388
7	311908.oc7	0.35	0.37	12.9	0.279
8	311930.oc7	0.38	0.34	12.8	0.265
9	311958.oc7	0.39	0.33	11.5	0.210
10	312021.oc7	0.40	0.39	13.7	0.303
11	312048.oc7	0.37	0.37	13.1	0.182
12	312111.oc7	0.40	0.25	9.3	0.087

13	312207.oc7	0.48	0.20	8.5	0.047
14	312232.oc7	0.50	0.22	9.0	0.077
15	312254.oc7	0.49	0.22	9.1	0.058
16	312316.oc7	0.49	0.21	8.6	0.086
17	312339.oc7	0.50	0.21	8.6	0.060
18	010004.no7	0.52	0.22	9.8	0.113
19	010030.no7	0.48	0.24	10.7	0.119
20	010055.no7	0.46	0.26	11.8	0.165
21	010140.no7	0.43	0.28	12.6	0.157
22	010204.no7	0.40	0.31	13.3	0.192
23	010226.no7	0.40	0.35	13.9	0.257
24	010248.no7	0.39	0.35	14.8	0.271
25	151238.de7	0.48	0.19	11.1	0.009
26	151301.de7	0.45	0.21	11.8	0.021

Table 2. Summary of wind and wave records: f_p , spectral peak frequency; H_s , significant wave height; U_{10} , wind speed at 10-m height; and b_r , visually observed dominant wave breaking probability.

b. Riding wave removal (RWR) processing of wave records

To measure breaking dissipation of Lake George waves through the passive acoustic method, we need to match each bubble-formation event with corresponding dominant breaking wave. In this study, each individual wave is defined as the surface elevations between two adjacent zero-upcrossings. In order to avoid the influence of riding waves on the determination of zero-upcrossings of dominant waves, the riding wave removal (RWR) technique (Banner et al. 2002; Schulz 2009) is employed. This non-spectral technique filters out small-scale riding waves without altering the large-scale dominant waves. This is achieved through an iterative procedure where the shortest wave in the record is identified (as consecutive local maxima and minima) and replaced by a reconstructed segment. The

iteration continues until all waves with frequency higher than a cutoff frequency f_c are removed. In Banner et al. (2002), f_c was first chosen as $1.9 f_p$ which was found to maximize the number of wave crests in the dominant wave band ($0.7 f_p - 1.3 f_p$). When applied to Lake George data, Schulz (2009) suggested a more conservative cutoff frequency ranged $2 f_p - 2.5 f_p$. In the present study, the cutoff frequency is set to be $2.5 f_p$. A comparison of the surface elevation records before and after RWR processing is shown in Fig. 6. The wave records after RWR processing will be used in the following work.

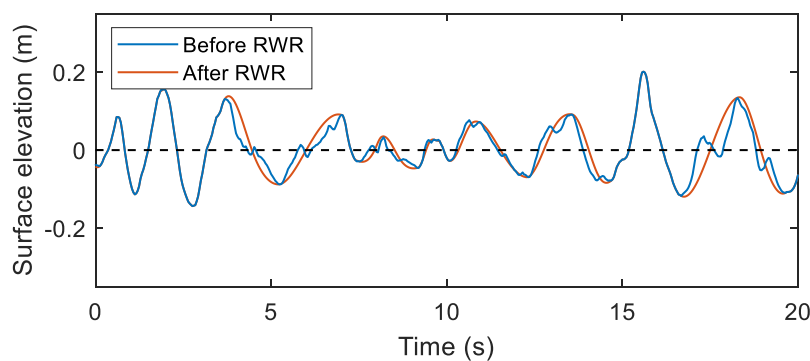


Fig. 6. Time series of surface elevation before and after RWR processing from record 9 of Table 2.

c. Wave breaking detection

Unlike in the laboratory, wave breakings occur randomly in the field environment. Before bubble size estimation, the wave breaking detection has to be conducted at first. Bass and Hay (1997) have found that breaking events generate crests in the sound spectrogram. Babanin et al. (2001) further demonstrated that the identification of distinct crests in the spectrograms, spanning a frequency range from 500 Hz to 4 kHz, appears to be a more reliable means of breaking detection in the complex spectral environment than the integrated ambient noise exceeding a threshold. In this paper, wave breakings were identified through the spectrograms of acoustic signals.

Following Babanin et al. (2001), the sound spectrogram is calculated as a time series of consecutive power spectral density (PSD), represented by $S(f, t)$, computed over every 256 readings (windowed with a Hanning window) of the acoustic signal with a 128-point overlap.

A typical spectrogram is shown in Fig. 7(a) where values of $S(f, t)$ are plotted in logarithmic scale, with dark stripes corresponding to spectrum crests.

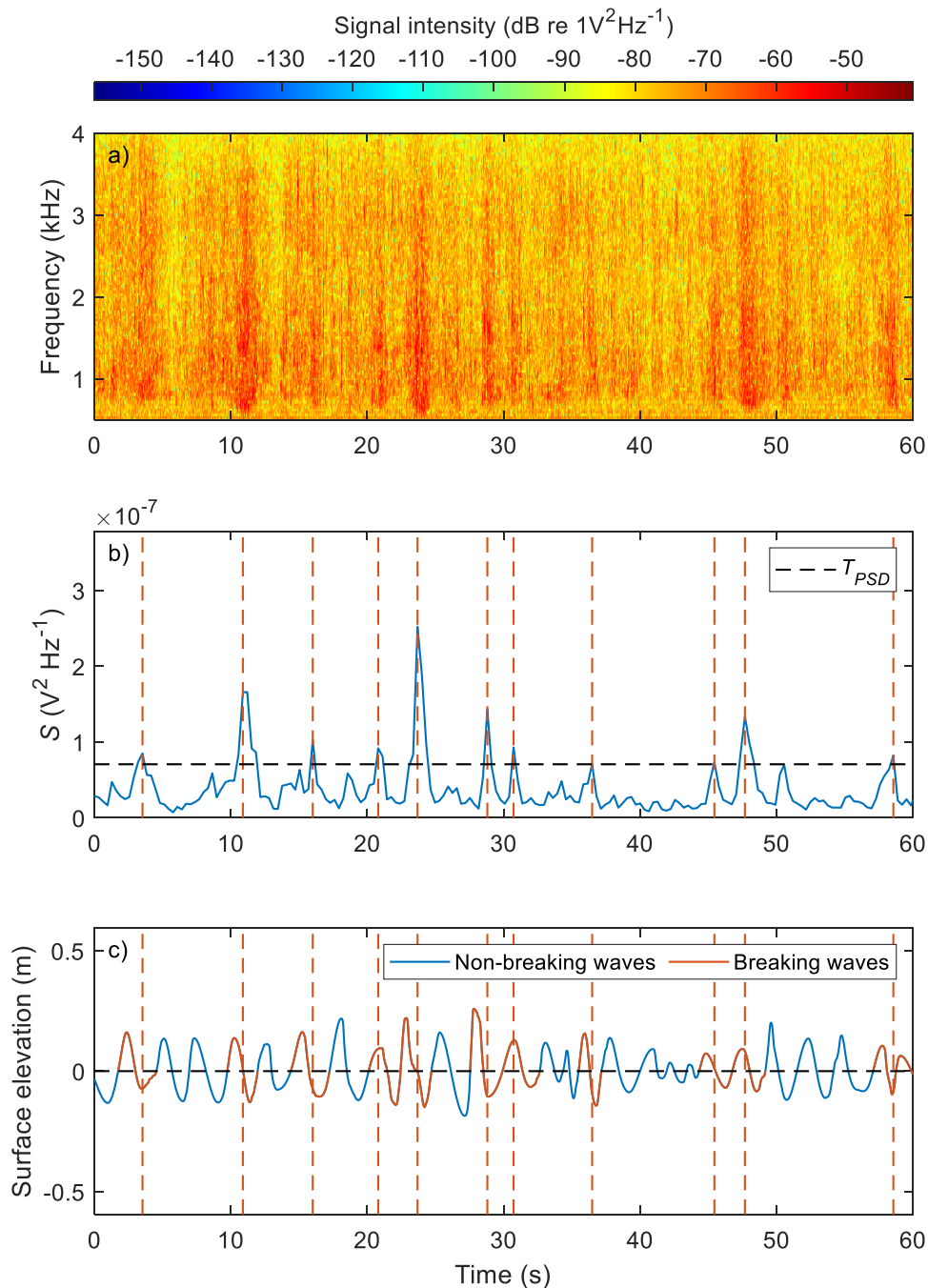


Fig. 7. Synchronized records. (a) Spectrogram of acoustic record. The colour contours represent signal intensity plotted in dB (the intensity is referenced to $1V^2Hz^{-1}$). (b) Time series of mean PSD $S(t)$. The PSD threshold T_{PSD} of this segment is shown as the horizontal dashed line. The vertical dashed lines indicate the locations of $S(t)$ peaks exceeding T_{PSD} .

(c) Time series of surface elevation. The waves identified as breakers are plotted in red. The data segments are taken from record 9 of Table 2.

In order to identify the breaking events through acoustic spectrogram, $S(f, t)$ is averaged over the frequency range of 0.5-4 kHz and then 20-point smoothed to obtain a time series of mean PSD $S(t)$. The time resolution of $S(t)$ is 0.32 s. In Fig. 7, the dark stripes in spectrogram (Fig. 7(a)) exhibit themselves as peaks in $S(t)$ (Fig. 7(b)) and can thus be captured by a proper PSD threshold, T_{PSD} . The value of T_{PSD} is determined by comparing the dominant wave breaking probability detected from $S(t)$ with the visually observed dominant wave breaking probability b_T listed in Table 2. In Babanin et al. (2001), b_T is defined as the ratio of the number of dominant breakers to Tf_p , where T is the time length of wave record. Within the period of an individual wave, if a $S(t)$ peak exceeding T_{PSD} is detected, this wave is regarded as a breaker. When the number of dominant breakers thus identified equals $b_T Tf_p$, this magnitude of T_{PSD} is chosen as the right one. The values of T_{PSD} of the 24 records are shown in Fig. 8 plotted versus b_T and significant wave height H_s , respectively. As expected, T_{PSD} rises with increasing b_T and H_s .

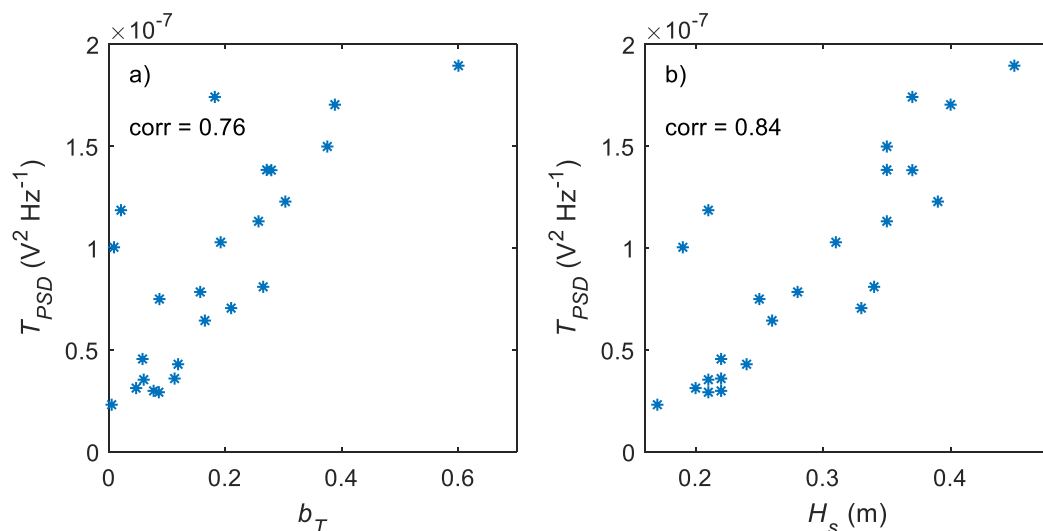


Fig. 8. PSD threshold T_{PSD} vs (a) dominant wave breaking probability b_T and (b) significant wave height H_s .

d. Bubble radius calculation

Like in the laboratory, the sound amplitude threshold T_A is used here to capture the high pulse groups over background noise. However, in field environment the background noise level at a given frequency may vary greatly, increasing with the wind speed (Knudsen et al. 1948). This fact makes a constant T_A no longer applicable in Lake George. In order to determine an appropriate T_A for each specific record, an empirical relationship between T_A and the RMS of acoustic records, χ , is established. The first 2-minute segments of each of the 24 acoustic records are taken for detailed inspection. Similar to the laboratory analysis, the value of T_A for each segment is set slightly higher than the upper envelope of nearly stationary background noise signals. The visually determined T_A against χ of all 24 acoustic records are plotted in Fig. 9 and the least-squares fitting yields

$$T_A = 1.21 \cdot 10^{-2} + 2.89 \chi . \quad (15)$$

In the following work, the value of T_A for each acoustic record is calculated according to Eq. (15).

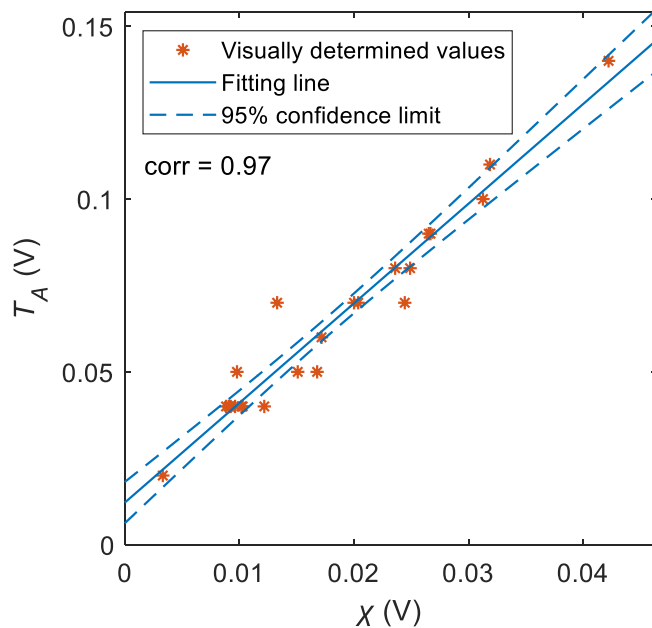


Fig. 9. Visually determined sound amplitude threshold T_A vs RMS of acoustic record χ . The best fit line (Eq. (15)) and 95% confidence limit are also shown.

As in the laboratory analysis, within the high pulse groups associated with wave breaking, there are also some long-period sound waves that seem irrelevant to bubble formation, although exceeding T_A . Therefore, the temporal steepness threshold T_S is also employed here. The proper values of T_S for all the 2-minute segments were visually determined and found, unexpectedly, to be almost the same, nearly 200 V s^{-1} . In Fig. 10, three typical segments of acoustic records corresponding to low, medium and high b_T are shown. The sound waves exceeding T_A with temporal steepness S_t higher and less than 200 V s^{-1} are drawn in red and yellow separately. It appears that the threshold $T_S = 200 \text{ V s}^{-1}$ works well in various wind and wave conditions.

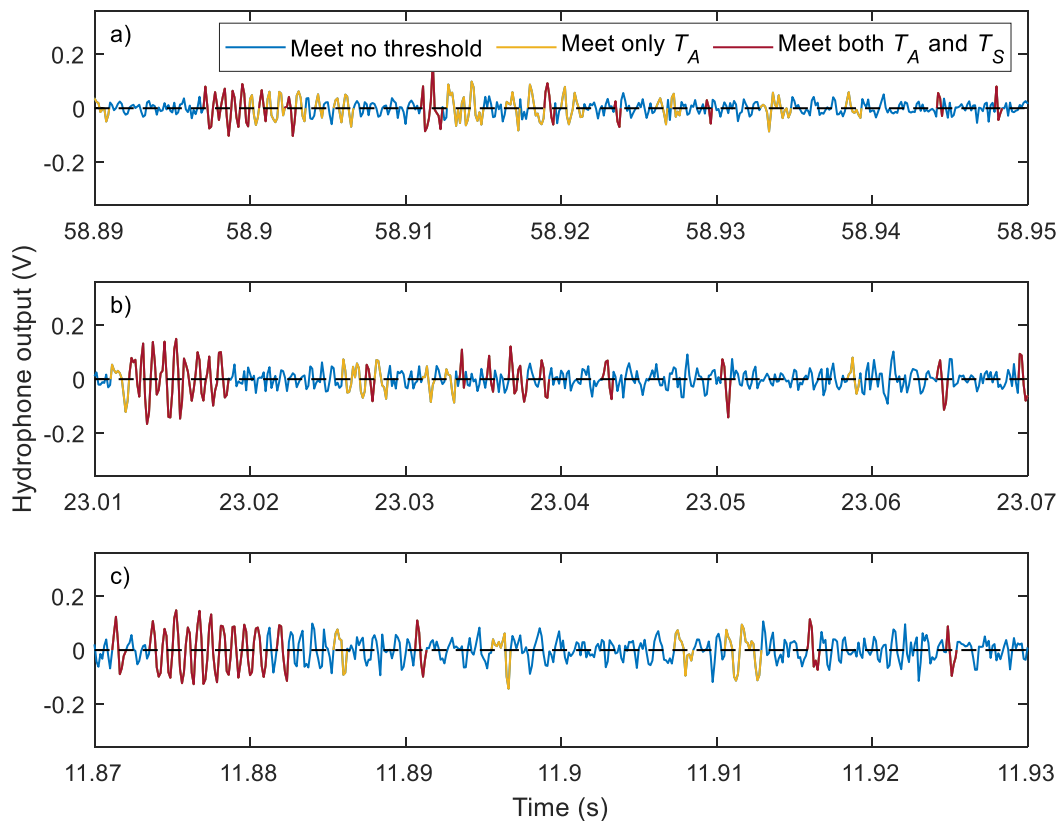


Fig. 10. Time series of hydrophone output from (a) record 18 with dominant wave breaking probability $b_T = 0.11$, (b) record 9 with $b_T = 0.21$ and (c) record 10 with $b_T = 0.30$.

The sound waves are selected by the amplitude threshold T_A (yellow) and further by the temporal steepness threshold T_S (red).

For each breaking wave, the acoustic signals between its start and end time are used for the bubble radius calculation. The frequencies of the sound waves meeting both T_A and T_S criteria were translated into bubble radii according to Eq. (2), then averaged to obtain the mean bubble radius R of this breaker. The observed size distributions of individual bubbles are shown in Fig. 11. Three records are selected to represent the wave breakings in Lake George with low, medium and high b_T . Similar to the laboratory measurements (Fig. 3), the bubble size distribution shifts to larger radius and becomes more concentrated as sea state grows. The sampling rate of 8 kHz in the Lake George experiment is able to resolve bubbles with radii greater than 0.82 mm. As shown in Fig. 11, the probability density of bubble radius is mainly concentrated below 2.5 kHz and is minimal when approaching the Nyquist frequency of 4 kHz. Therefore, the sampling rate 8 kHz is sufficient for the present study.

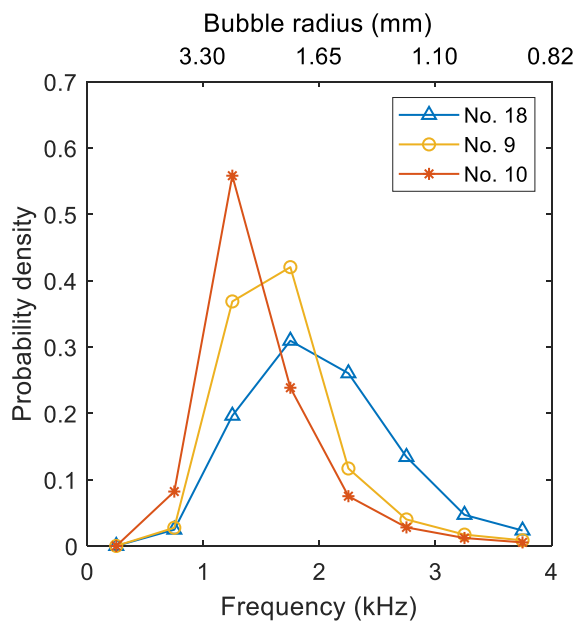


Fig. 11. Size distributions of individual bubbles measured in Lake George. The blue, yellow and red lines correspond to record No. 18, 9 and 10 of Table 2, respectively.

For each 20-minute record, the mean value of R , denoted by R_m , is taken as a proxy of mean breaking severity. In Fig. 12(a), R_m versus b_T is plotted as circles for the 24 records. The rise of R_m with increasing b_T is rapid at $b_T < 0.1$ then slows down at large b_T . Therefore, an exponential function fit was adopted, which yields

$$R_m = (1.20 + 2.14 \cdot b_T^{0.47}) \cdot 10^{-3}. \quad (16)$$

The sensitivity of Eq. (16) to T_s is also examined here. The results with $T_s = 200 \text{ V s}^{-1}$ and $T_s = 240 \text{ V s}^{-1}$ are compared in Fig. 12(b) which shows that the fitting coefficient and exponent are not very sensitive to the value of T_s .

Eq. (16) has an offset which makes it irrational, since R_m is expected to be zero when no breaking occurs. For the same reason as mentioned in section 2b, the offset is regarded as a systematic error coming from the bubble detection method. The actual R of each breaking wave is approximated as the measured value minus $1.20 \cdot 10^{-3} \text{ m}$. The relationship between R_m and b_T is thus calibrated to be

$$R_m = 2.14 \cdot 10^{-3} b_T^{0.47}. \quad (17)$$

Eq. (17) is close to quadratic and therefore a quadratic fitting is also made here, which gives

$$R_m = 2.22 \cdot 10^{-3} b_T^{0.5}. \quad (18)$$

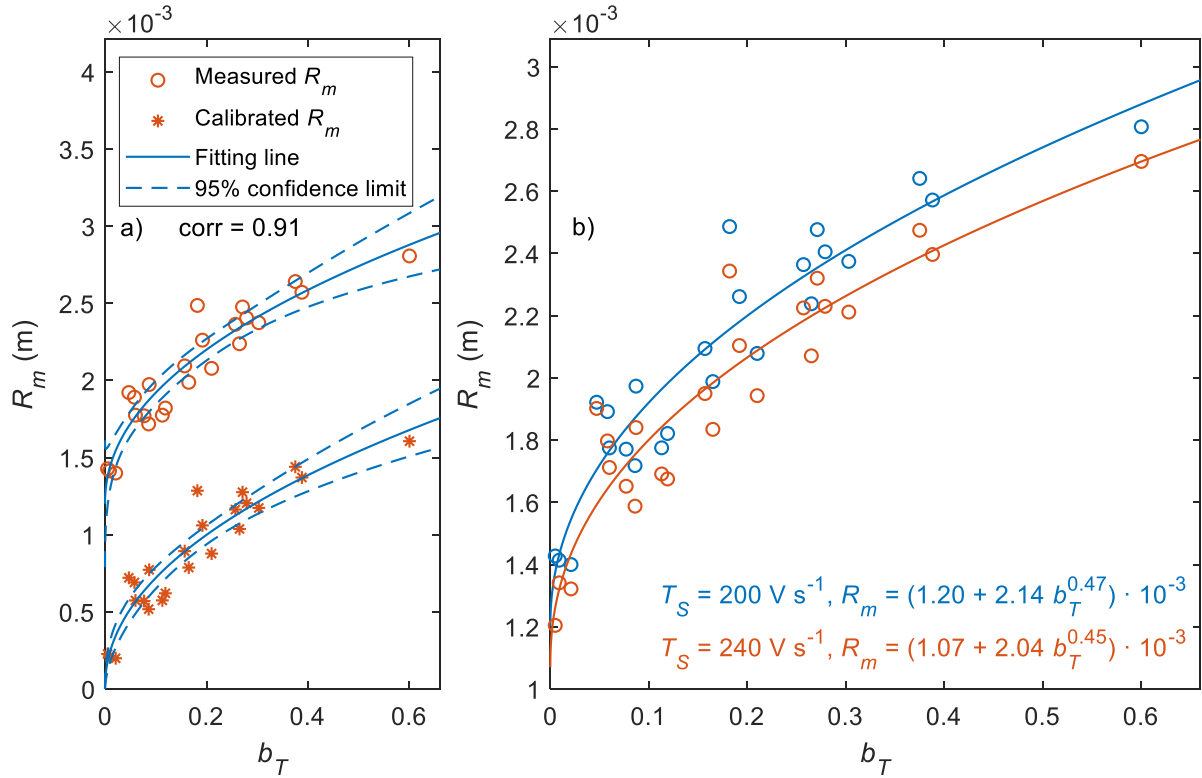


Fig. 12. (a) Field measured mean bubble radius R_m (o) and its calibrated counterpart (*) vs the dominant wave breaking probability b_T . The upper and lower fitting lines correspond to Eq. (16) and Eq. (17), respectively. The 95% confidence limits are shown with dashed lines. (b) Sensitivity test of Eq. (16) for the temporal steepness threshold T_S . The blue and red colours correspond to $T_S = 200 \text{ V s}^{-1}$ and $T_S = 240 \text{ V s}^{-1}$, respectively.

According to Eq. (14), R_m are converted into the mean breaking severity ΔE_m . The ratio between ΔE_m and the zeroth spectral moment m_0 may be taken as a representation of the mean relative energy loss of the breakers in each record. In Fig. 13(a), $\Delta E_m/m_0$ is plotted against b_T .

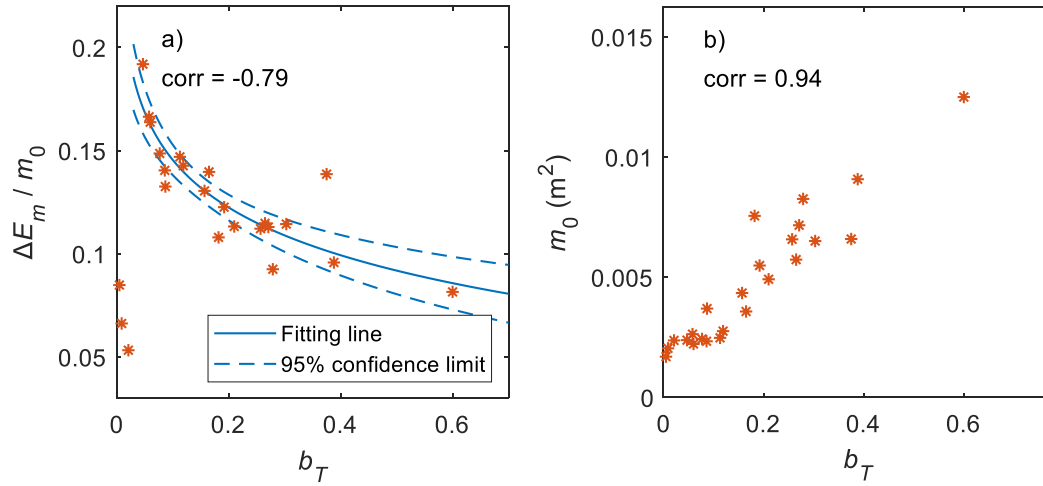


Fig. 13. (a) The relative wave energy loss $\Delta E_m/m_0$ vs the dominant wave breaking probability b_T . The best fit line (Eq. (19)), 95% confidence limit and the correlation coefficient in range $b_T > 0.03$ are also shown. (b) The zeroth spectral moment m_0 vs b_T .

As shown in Fig. 12(a) and Fig. 13(b), when $b_T < 0.1$, R_m grows rapidly with b_T while m_0 keeps almost constant. Consequently, in Fig. 13(a) $\Delta E_m/m_0$ exhibits a leap when b_T exceeds about 0.03. Similar feature was also reported by Rapp and Melville (1990). In their Fig. 15, the breaking severity shows a sharp rise as wave steepness increases once it exceeds a critical value where the incipient breaking was observed to occur. At $b_T > 0.03$, $\Delta E_m/m_0$ decrease quickly in the low b_T range and the rate of decline slows down in the medium to high b_T range. For the records with $b_T > 0.03$, $\Delta E_m/m_0$ range from about 8% to 20%. The best fitting of the datapoints with $b_T > 0.03$ gives

$$\frac{\Delta E_m}{m_0} = 28.0 - 27.9b_T^{1.20 \cdot 10^{-3}} \quad (19)$$

which is also shown in Fig. 13(a).

4. Breaking spectral dissipation

a. Acoustic determination of spectral dissipation

In section 3, we have identified the breaking waves and obtained their corresponding bubble radii. From the wave records after RWR processing, the zero-upcrossing periods of

these breaking waves are read. These data are combined to investigate the frequency distribution of breaking dissipation. The frequency range studied here is $0.7 f_p - 2.1 f_p$. It is uniformly divided into seven bands

$$f = f_i \pm 0.1 f_p \quad (i=1, 2 \dots 7) \quad (20)$$

with the set of central frequencies being $f_i = (0.8 + 0.2(i-1)) f_p$. The breakers together with their corresponding bubble radii are grouped into the seven frequency bands. Since the breaking waves in the records with very low b_T are too few to ensure statistical stability when they are allocated into seven bands, only the 15 records with $b_T \geq 0.1$ are used in the following analysis.

Within each frequency band, the spectral dissipation rate $D_a(f)$ is calculated according to

$$D_a(f) = -\frac{\Delta \bar{E}_i \cdot P_i}{\Delta f} \quad (21)$$

where the subscript a in $D_a(f)$ refers to the acoustic technique, $\Delta \bar{E}_i$ is the mean breaking severity in this band,

$$\Delta \bar{E}_i = \frac{\sum_{j=1}^{n_i} \Delta E_j}{n_i}, \quad (22)$$

P_i is the breaking probability in this band,

$$P_i = \frac{n_i}{T}, \quad (23)$$

$\Delta f = 0.2 f_p$ is the bandwidth, n_i is the number of breakers in this band, ΔE_j is the breaking severity of the j^{th} breaker in this band, and $T = 1200$ s is the time length of the wave record. The breaking severity ΔE_j is calculated from mean bubble radius R according to Eq. (14). The spectral dissipation rates $D_a(f)$ of the 15 records thus calculated are plotted in Fig. 14 together with the wave spectrum $F(f)$. It can be seen that most of the energy dissipation occurs around the spectral peak. This feature may be explained as follows. Firstly, the wind waves measured in the depth-limited Lake George are well developed and even fully

developed, in which the wind input, nonlinear interaction and breaking dissipation are approximately in balance. Under the influence of bottom interaction, the transfer of energy to low frequencies due to wind input and nonlinear interaction could be more effective compared to comparable deep-water cases, result in greater breaking dissipation of long waves (Young and Verhagen 1996). Secondly, the acoustic spectrogram analysis employed in this paper is expected to be reliable in detecting dominant breakers. The acoustic signature of short breakers would be too weak to be identified. Even if such a breaker is detected, the breaking event might be credited to the underlying dominant wave rather than the short wave itself. As a result, the dissipation at high frequencies would be underestimated.

Another overall feature of $D_a(f)$ curve is its similarity to $F(f)$ curve, which indicates a possible linear relationship between the two functions.

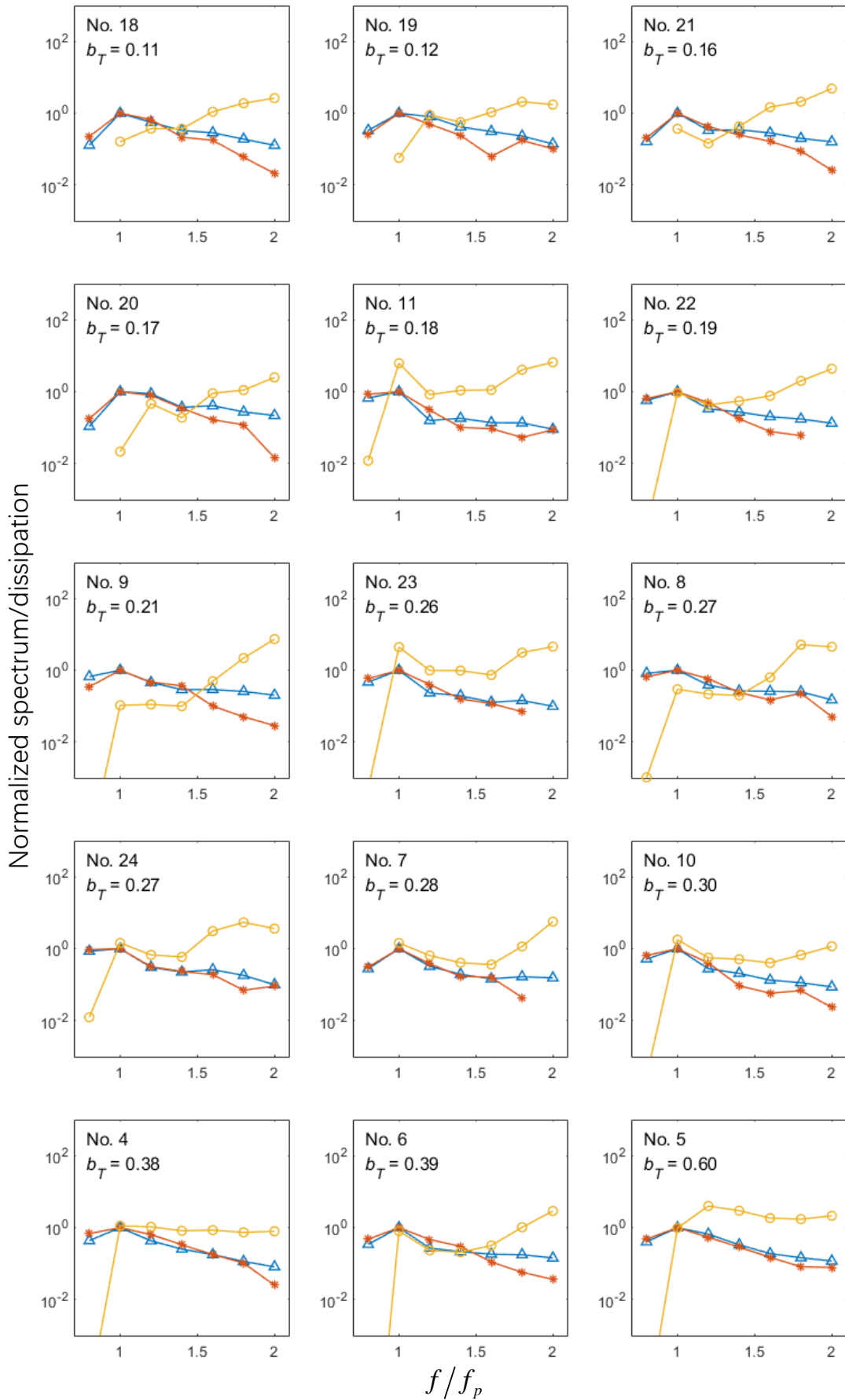


Fig. 14. Comparison between the experimental spectral dissipation $D_a(f)$ (-*) (Eq. (21)) and the ST6 dissipation function $D_{ST6}(f)$ (-o) of all the 15 Lake George records with dominant wave breaking probability $b_T \geq 0.1$. Both $D_a(f)$ and $D_{ST6}(f)$ are normalized by $D_a(f_p)$. The blue line (-Δ) is the wave spectrum $F(f)$ normalized by $F(f_p)$. The subgraphs are arranged in order of b_T .

b. Verification of the acoustic approach

To examine the reliability of the acoustic method, the spectral dissipation rate $D_a(f)$ calculated in the present paper is compared with its counterpart in YB06. In their work, the spectral dissipation rate of the record 311823.oc7 (No. 5 in Table 2) with a dominant wave breaking probability $b_T = 0.60$ was estimated through direct approaches. The wave record was divided into five incipient breaking segments and four post breaking segments. The incipient breaking segments were used to obtain the “incipient breaking spectrum” $F_i(f)$ and the post breaking segments were used to obtain the “post breaking spectrum” $F_p(f)$. The difference $\Delta F = F_p(f) - F_i(f)$ is attributed to breaking dissipation and the spectral dissipation rate is estimated by

$$S_{ds}(f) = g \frac{\Delta F}{\Delta t} \quad (24)$$

where Δt is the time difference between the mean time points of subsequent breaking and nonbreaking segments. The integral energy dissipation is

$$\int_f S_{ds}(f) df = -1.1 \cdot 10^{-4} m^3 s^{-3}. \quad (25)$$

YB06 also studied the velocity spectra measured by Acoustic Doppler Velocimeter (ADV). The difference between the depth-integrated turbulent dissipation rate before and after breaking, ΔD , is attributed to wave breaking dissipation. They found $\Delta D = -1.0 \cdot 10^{-4} m^3 s^{-3}$, matching remarkably well with $\int_f S_{ds}(f) df$. As pointed by YB06, both of their approaches yield a lower-bound estimate of wave breaking dissipation. For the spectrum difference ΔF , this is because the incipient breaking waves have already lost some wave energy and the post breaking waves have gained some wind input, before they arrive at the measuring point. For

the ADV measured ΔD , this is due to the fact that some of the lost wave energy is expended on work against buoyancy forces while entraining bubbles into the water, rather than on generating the turbulence. According to Melville et al. (1992), the fraction of the breaking dissipation lost in entraining the air can be up to 30%-50% of the total. Consequently, the actual dissipation rate shall be approximately within $-(1.4 \sim 2.0) \cdot 10^{-4} m^3 s^{-3}$.

In order to be consistent with YB06, here the dissipation rate $D_a(f)$ is multiplied by g . The integrated dissipation rate calculated in the present paper is

$$g \int_{0.7f_p}^{2.1f_p} D_a(f) df = -1.9 \cdot 10^{-4} m^3 s^{-3} \quad (26)$$

which falls in the range of $-(1.4 \sim 2.0) \cdot 10^{-4} m^3 s^{-3}$ and thus validates the rationality of the acoustic method to some extent. It should be noted that Eq. (25) covers a broader frequency range than Eq. (26). Since the energy loss is mainly contributed by dominant breaking, this difference can be neglected.

YB06 also noticed the similarity between spectral dissipation and wave spectrum. They first investigated the possible linear relationship between the spectral dissipation rate $S_{ds}(f)$ and incipient breaking spectrum $F_i(f)$ and found

$$S_{ds}(f) = -2.0 \cdot 10^{-3} [gF_i(f)]^{1.01} \approx -1.6 \cdot 10^{-3} gF_i(f). \quad (27)$$

The proportionality coefficient in Eq. (27) is dimensional. Therefore, they also provided a general relationship between $S_{ds}(f)$ and $fF_i(f)$,

$$S_{ds}(f) = -1.8 \cdot 10^{-2} [gfF_i(f)]^{1.47}. \quad (28)$$

In the present paper, $F_i(f)$ is replaced by $F(f)$ since the former is unknown and the latter is commonly used in wave models. In Fig. 15, $gD_a(f)$ is plotted against $gF(f)$ and $gfF(f)$, respectively. It is worth noting that the datapoints at $f = 0.8f_p$ (marked as the two circles in Fig. 15(a) and (b)) deviate distinctly from the overall trends. Considering the depth-limited condition in Lake George, the breaking of long waves could be significantly enhanced by the wave-bottom interaction. Therefore, the simple functional forms of Eq. (27) and Eq. (28) are not adequate for this case. If we exclude the datapoints at $f = 0.8f_p$, the least-squares fittings yield

$$gD_a(f) = -2.1 \cdot 10^{-3} [gF(f)]^{1.22} \approx -1.8 \cdot 10^{-3} gF(f) \quad (29)$$

and

$$gD_a(f) = -2.0 \cdot 10^{-2} [gfF(f)]^{1.80} \approx -2.9 \cdot 10^{-2} [gfF(f)]^2 \quad (30)$$

which are also shown in Fig. 15.

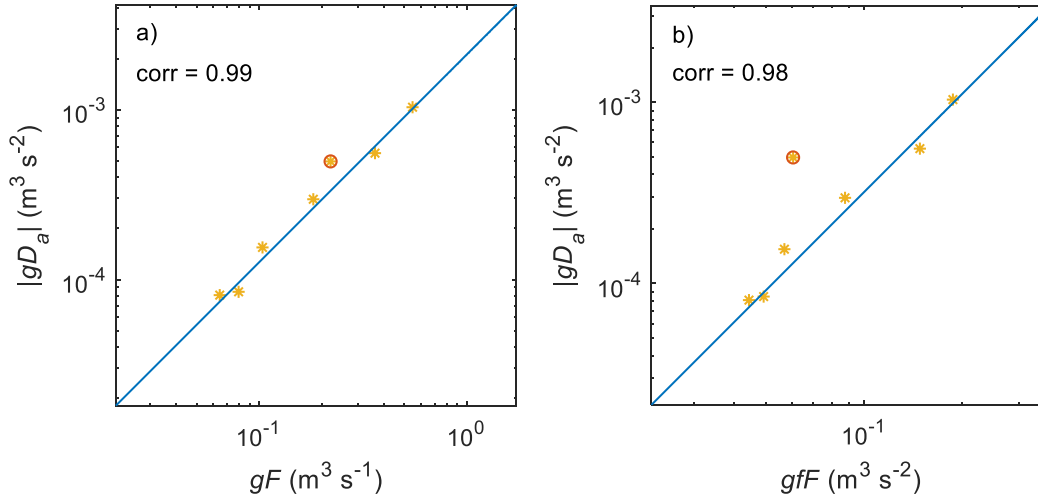


Fig. 15. (a) Spectral breaking dissipation rate gD_a vs gF and the best fit line (Eq. (29)). (b) gD_a vs gfF and the best fit line (Eq. (30)). The datapoints at $f = 0.8f_p$ are marked as circles and are excluded in the calculation of correlation coefficients.

The discrepancy between the two linear dependences in Eq. (27) and Eq. (29) mainly comes from the underestimation of $S_{ds}(f)$ as mentioned above. Moreover, using $F(f)$ instead of $F_i(f)$ in spectral dissipation functions may also introduce minor deviations. YB06 found that the mean energy loss across the full measured spectrum of the record 311823.oc7 is about 20%. Therefore, $F(f)$ is about 90% of $F_i(f)$ and the linear relationship of Eq. (27) can be approximately rewritten as

$$S_{ds}(f) \approx -1.8 \cdot 10^{-3} gF(f). \quad (31)$$

which makes it the same as Eq. (29). Although YB06 and the present work calculate the spectral dissipation in absolutely different ways, the two studies obtained very close results given the very large uncertainties in the measurements.

To further validate the acoustic method, a series of comparisons are made between $D_a(f)$ and the ST6 source functions. The ST6 source term package is developed based on observations and it has been implemented in both WAVEWATCH III and SWAN model. The reader is referred to Rogers et al. (2012), Zieger et al. (2015) and the references therein for more details. Here we only briefly describe the wave breaking term S_{ds} of the ST6 package.

The ST6 whitecapping dissipation function S_{ds} incorporates two different mechanisms. The first is the inherent wave breaking $T_1(k, \theta)$ taking effect in the whole frequency range once a spectral density threshold is exceeded (Banner et al. 2000; Babanin et al. 2001). The second is the induced breaking $T_2(k, \theta)$ of relatively short waves due to modulation of longer waves occurring only beyond the spectral peak (Donelan 2001; YB06). Here θ is wave direction. For one-dimensional wave, the breaking dissipation rate S_{ds} in terms of frequency is expressed as

$$S_{ds} = T_1(f) + T_2(f), \quad (32)$$

$$T_1(f) = a_1 f \left[\frac{\Delta(f)}{F_T(f)} \right]^{p_1}, \quad (33)$$

$$T_2(f) = a_2 \left\{ \int_{f_{\min}}^f \left[\frac{\Delta(f)}{F_T(f)} \right]^{p_2} df \right\} F(f) \quad (34)$$

where a_1 , a_2 , p_1 and p_2 are tunable parameters, f_{\min} is the lowest modeled frequency, $F_T(f) = (B_T/k^3) dk/df$ is the spectral density threshold, $B_T = 0.035^2$ is the dimensionless saturation-threshold value, k is wavenumber, $\Delta(f) = F(f) - F_T(f)$ is the exceedance level. In the present study, the tunable parameters are set as the default values in WAVEWATCH III, $a_1 = 4.75 \cdot 10^{-6}$, $a_2 = 7.00 \cdot 10^{-5}$ and $p_1 = p_2 = 4$.

The spectral dissipation rates of the 15 Lake George records are calculated according to ST6 functions. These results, represented by D_{ST6} , are also plotted in Fig. 14 for comparison. In general, the magnitudes of D_a and D_{ST6} are comparable within the range $0.9f_p - 1.3f_p$. Out of this frequency range, their discrepancy is rather significant. While D_a consistently

exhibits a considerable value around $0.8f_p$, D_{ST6} is negligible or even becomes zero. This difference mainly comes from the fact that ST6 is designed for the ocean environment and the wave-bottom interaction in the depth-limited condition is not considered. At $f > 1.3f_p$, D_{ST6} is much higher than D_a . Although the possible underestimation of D_a at high frequency mentioned above explains part of the difference, the huge discrepancy is thought to originate mainly from the wind input term of ST6. Compared with the traditional parameterizations, the wind input term of ST6 is remarkably larger at high frequencies (Zieger et al. 2015) and a greater whitecapping dissipation is needed to balance the total energy. Additionally, the default set of tunable parameters used here are determined for ocean waves. They may also bring errors to Lake George waves.

To illustrate quantitatively the difference between D_a and D_{ST6} within $0.9f_p - 1.3f_p$, the ratios between D_a and D_{ST6} ,

$$R_D(f) = \frac{D_a(f)}{D_{ST6}(f)} \quad (35)$$

are calculated at f_p and $1.2f_p$. As illustrated in Fig. 16, while $R_D(f_p)$ gradually approaches 1 as b_T increases, $R_D(1.2f_p)$ shows no obvious dependence on b_T . Most of the datapoints fall into the range of [0.1,10], indicating that there is no contradiction in magnitude between D_a and D_{ST6} within $0.9f_p - 1.3f_p$.

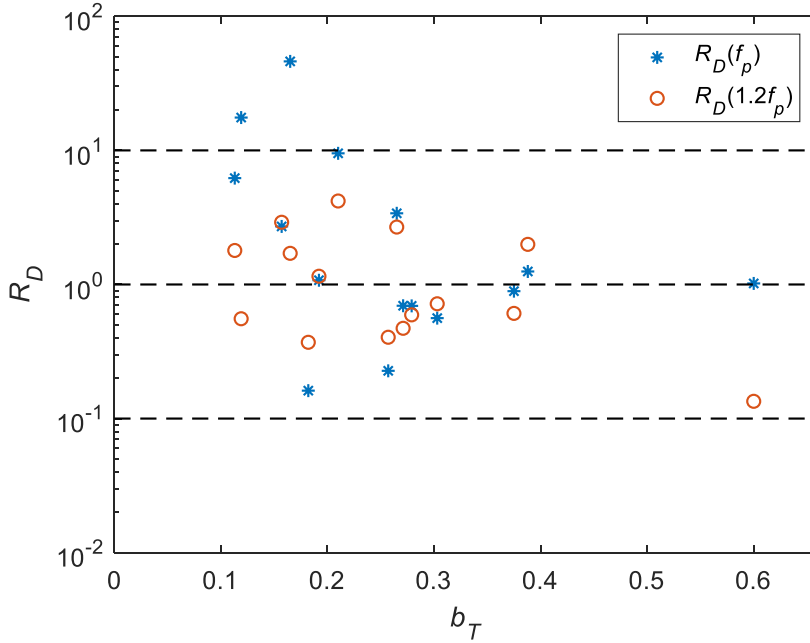


Fig. 16. R_D (Eq. (35)) at f_p (*) and $1.2f_p$ (o) vs the dominant wave breaking probability b_T .

5. Conclusions

In this study, we attempted to estimate the spectral breaking (whitecapping) dissipation in wave field through a passive acoustic method. In order to achieve this, we need to know the breaking severity (i.e. how much energy is lost in a single breaking event) and breaking probability (i.e. how many such events happen per unit of time) separately across different spectral bands.

The breaking severity ΔE is associated with the mean radius R of the bubbles generated during breaking. The latter can be derived from hydrophone record. To find the relationship between ΔE and R , laboratory experiments were carried out and a linear empirical formula was established. Dimensional analysis was also conducted and a relationship between nondimensional mean bubble radius \tilde{R} and nondimensional breaking severity $\tilde{\Delta E}$ was suggested. The laboratory relationship was then applied to Lake George data to calculate ΔE of field breakers.

The breaking events in Lake George were identified through a sound spectrogram method. For each detected breaker, the corresponding mean bubble radius was calculated and

translated into breaking severity. Meanwhile, the periods of the breaking waves were read from the wave record and thus the breakers as well as their breaking dissipations could be attributed to different spectral bands, and the spectral dissipation was finally obtained.

The maximum of the spectral breaking dissipation D_a in Lake George was found to occur around the peak frequency of the wave spectrum. For field record No. 5 of Table 2, D_a was compared with the direct estimates obtained by YB06, who used two completely different methods. Our estimates are in good agreement both quantitatively and qualitatively with YB06 which gives us confidence in the estimates of magnitudes of such a complicated process. Furthermore, for the 15 field records with $b_T > 0.03$, D_a are compared with the breaking dissipation source terms ST6 (WAVEWATCH-III model). Generally, D_a are of the same order as the ST6 breaking dissipation function D_{ST6} in the frequency band $0.9f_p - 1.3f_p$.

Although there are still some embedded uncertainties to be refined, this preliminary application of passive acoustic method has yielded many encouraging results. Further applications on more extensive datasets are to be carried out to validate and advance this methodology.

Acknowledgments.

We thank two anonymous reviewers for their useful comments and suggestions that improved the manuscript. XZ is supported by the China Scholarship Council (CSC). AVB acknowledges support of the US Office of Naval Research Global, Grant Number N62909-20-1-2080.

Data Availability Statement.

The data that support the findings of this study can be accessed online ([10.5281/zenodo.5778384](https://doi.org/10.5281/zenodo.5778384)).

APPENDIX

Symbol list

E_b	Wave energy density before breaking
E_a	Wave energy density after breaking
s	Severity coefficient defined in Eq. (1).
ω_0	Radian frequency of bubble oscillation
γ	Ratio of specific heats of the gas
p_0	Absolute liquid pressure
ρ	Liquid density
R_0	Equivalent spherical radius of the bubble
H	Wave height
f	Wave frequency
T_A	Sound amplitude threshold
S_t	Temporal steepness defined in Eq. (3).
H_{sw}	Sound wave height
T_{sw}	Sound wave period
T_S	Temporal steepness threshold
R	Mean bubble radius of an individual breaking wave
ρ_w	Water density
g	Gravitational acceleration
ΔE	Breaking severity defined in Eq. (4).
T	Time length of a wave record
ζ_u	Surface elevations measured upstream of the breaking point

ζ_d	Surface elevations measured downstream of the breaking point
ρ_a	Air density
σ	Surface tension coefficient
\tilde{R}	Dimensionless mean bubble radius defined in Eq. (8)
$\Delta\tilde{E}$	Dimensionless breaking severity defined in Eq. (9)
$\tilde{\rho}$	Dimensionless density defined in Eq. (10)
f_p	Spectral peak frequency
H_s	Significant wave height
U_{10}	Wind speed at 10-m height
b_T	Visually observed dominant wave breaking probability
f_c	Cutoff frequency employed in RWR processing
S	Power spectral density (PSD) of sound spectrogram
T_{PSD}	PSD threshold
χ	RMS of acoustic records
R_m	Mean bubble radius over a 20-minute field record
ΔE_m	Mean breaking severity over a 20-minute field record
m_0	Zeroth spectral moment
$D_a(f)$	Experimental spectral dissipation
$\Delta\bar{E}_i$	Mean breaking severity in the i^{th} frequency band
P_i	Breaking probability in the i^{th} frequency band
Δf	Bandwidth of the frequency band

n_i	The number of breakers in the i^{th} frequency band
$F(f)$	Wave spectrum
$D_{ST6}(f)$	ST6 dissipation function
$F_i(f)$	Incipient breaking spectrum
$F_p(f)$	Post breaking spectrum
ΔF	Spectral energy loss obtained by YB06
$S_{ds}(f)$	Spectral dissipation rate
Δt	Time difference between the mean time points of subsequent breaking and nonbreaking segments
ΔD	Difference between the depth-integrated turbulent dissipation rate before and after breaking
T_1	Inherent wave breaking term of ST6
T_2	Induced wave breaking term of ST6
θ	Wave direction
a_1, a_2, p_1 and p_2	Tunable parameters in ST6 dissipation function
f_{\min}	Lowest modeled frequency in ST6 dissipation function
$F_T(f)$	Spectral density threshold in ST6 dissipation function
B_T	Dimensionless saturation-threshold value
k	Wavenumber
$\Delta(f)$	Exceedance level in ST6 dissipation function
$R_D(f)$	Ratio between D_a and D_{ST6}

REFERENCES

- Babanin, A., 2011: *Breaking and dissipation of ocean surface waves*. Cambridge University Press, 480 pp, <https://doi.org/10.1017/CBO9780511736162>.
- Babanin, A. V., I. R. Young, and M. L. Banner, 2001: Breaking probabilities for dominant surface waves on water of finite constant depth. *J. Geophys. Res.: Oceans*, **106**, 11659-11676, <https://doi.org/10.1029/2000jc000215>.
- Babanin, A.V., T. Waseda, T. Kinoshita, and A. Toffoli, 2011: Wave breaking in directional fields. *J. Phys. Oceanogr.*, **41**, 145-156, <https://doi.org/10.1175/2010jpo4455.1>.
- Banner, M. L., A. V. Babanin, and I. R. Young, 2000: Breaking probability for dominant waves on the sea surface. *J. Phys. Oceanogr.*, **30**, 3145-3160, [https://doi.org/10.1175/1520-0485\(2000\)030<3145:bpfdwo>2.0.co;2](https://doi.org/10.1175/1520-0485(2000)030<3145:bpfdwo>2.0.co;2).
- Banner, M. L., J. R. Gemmrich, and D. M. Farmer, 2002: Multiscale measurements of ocean wave breaking probability. *J. Phys. Oceanogr.*, **32**, 3364-3375, [https://doi.org/10.1175/1520-0485\(2002\)032<3364:mmoowb>2.0.co;2](https://doi.org/10.1175/1520-0485(2002)032<3364:mmoowb>2.0.co;2).
- Bass, S. J., and A. E. Hay, 1997: Ambient noise in the natural surf zone: wave-breaking frequencies. *IEEE J. Oceanic Eng.*, **22**, 411-424, <https://doi.org/10.1109/48.611130>.
- Buckingham, E., 1914: On physically similar systems; illustrations of the use of dimensional equations. *Phys. Rev.*, **4**, 345-376, <https://doi.org/10.1103/physrev.4.345>.
- Chanson, H., R. Manasseh, 2003: Air entrainment processes in a circular plunging jet: Void-fraction and acoustic measurements. *J. Fluids Eng.*, **125**, 910-921, <https://doi.org/10.1115/1.1595672>.
- Chen, L., R. Manasseh, A. Nikolovksa, and C. Norwood, 2003: Noise generation by an underwater gas jet. *Proc. Eighth Western Pacific Acoustics Conf.*, Melbourne, Australia, WC21_1-4.
- Deane, G. B., and M. D. Stokes, 2002: Scale dependence of bubble creation mechanisms in breaking waves. *Nature*, **418**, 839-844, <https://doi.org/10.1038/nature00967>.
- Deane, G. B., and M. D. Stokes 2008: The acoustic excitation of air bubbles fragmenting in sheared flow. *J. Acoust. Soc. Am.*, **124**, 3450-3463, <https://doi.org/10.1121/1.3003076>.
- Donelan, M. A., 2001: A nonlinear dissipation function due to wave breaking. *Proc. ECMWF Workshop on Ocean Wave Forecasting*, 87-94.

- Felizardo, F. C., and W. K. Melville, 1995: Correlations between ambient noise and the ocean surface wave field. *J. Phys. Oceanogr.*, **25**, 513-532 [https://doi.org/10.1175/1520-0485\(1995\)025<0513:cbanat>2.0.co;2](https://doi.org/10.1175/1520-0485(1995)025<0513:cbanat>2.0.co;2).
- Hwang, P. A., D. Xu, and J. Wu, 1989: Breaking of wind-generated waves: Measurements and characteristics. *J. Fluid Mech.*, **202**, 177-200, <https://doi.org/10.1017/s002211208900114x>.
- Kerman, B. R., 2012: *Natural Physical Sources of Underwater Sound: Sea Surface Sound* (2). Springer Science & Business Media, 480 pp, <https://doi.org/10.1007/978-94-011-1626-8>.
- Knudsen, V. O., R. S. Alford, and J. W. Emling, 1948: Underwater ambient noise. *J. mar. Res.*, **7**, 410-429.
- Kway, J. H., Y. S. Loh, and E. S. Chan, 1998: Laboratory study of deep-water breaking waves. *Ocean Eng.*, **25**, 657-676, [https://doi.org/10.1016/s0029-8018\(97\)00039-5](https://doi.org/10.1016/s0029-8018(97)00039-5).
- Liberzon, D., A. Vreme, S. Knobler, and I. Bentwich, 2019: Detection of breaking waves in single wave gauge records of surface elevation fluctuations. *J. Atmos. Oceanic Technol.*, **36**, 1863-1879, <https://doi.org/10.1175/jtech-d-19-0011.1>.
- Liu, P.C., and A.V. Babanin, 2004: Using wavelet spectrum analysis to resolve breaking events in the wind wave time series. *Ann. Geophys.*, **22**, 3335-3345, <https://doi.org/10.5194/angeo-22-3335-2004>
- Loewen, M. R., and W. K. Melville, 1991: Microwave backscatter and acoustic radiation from breaking waves. *J. Fluid Mech.*, **224**, 601-623, <https://doi.org/10.1017/s0022112091001891>.
- Lu, N. Q., A. Prosperetti, and S. W. Yoon, 1990: Underwater noise emissions from bubble clouds. *IEEE J. Oceanic Eng.*, **15**, 275-281, <https://doi.org/10.1109/48.103521>.
- Manasseh, R., 1997: Acoustic sizing of bubbles at moderate to high bubbling rates. *Experimental Heat Transfer, Fluid Mechanics and Thermodynamics*, Brussels, Belgium, 943-947.
- Manasseh, R., 2021: *Fluid Waves*. CRC Press, 312 pp, <https://doi.org/10.1201/9780429295263>.

- Manasseh, R., A. V. Babanin, C. Forbes, K. Rickards, I. Bobevski, and A. Ooi, 2006: Passive acoustic determination of wave-breaking events and their severity across the spectrum. *J. Atmos. Oceanic Technol.*, **23**, 599-618, <https://doi.org/10.1175/jtech1853.1>.
- Medwin, H., and M. M. Beaky, 1989: Bubble sources of the Knudsen sea noise spectra. *J. Acoust. Soc. Am.*, **86**, 1124-1130, <https://doi.org/10.1121/1.398104>.
- Melville, W. K., M. R. Loewen, and E. Lamarre, 1992: Sound production and air entrainment by breaking waves: A review of recent laboratory experiments. *Breaking Waves-IUTAM Symposium*, 139-146, https://doi.org/10.1007/978-3-642-84847-6_11.
- Meza, E., J. Zhang, and R. J. Seymour, 2000: Free-wave energy dissipation in experimental breaking waves. *J. Phys. Oceanogr.*, **30**, 2404-2418, [https://doi.org/10.1175/1520-0485\(2000\)030<2404:fwedie>2.0.co;2](https://doi.org/10.1175/1520-0485(2000)030<2404:fwedie>2.0.co;2).
- Minnarert, M., 1933: On musical air-bubbles and the sounds of running water. *London Edinburgh Dublin Philos. Mag. J. Sci. Series 7*, **16**, 235-248, <https://doi.org/10.1080/14786443309462277>.
- Munk, W. H., 1947: A critical wind speed for air-sea boundary processes. *J. mar. Res.*, **6**, 203.
- Nelli, F., G. Deane, A. Ooi, and R. Manasseh, 2022: Analysis of sound pressure levels generated by nozzle-emitted large bubbles. *JASA Express Letters*, **2**, 054002, <https://doi.org/10.1121/10.0010377>.
- Pandit, A. B., J. Varley, R. B. Thorpe, and J. F. Davidson, 1992: Measurement of bubble size distribution: an acoustic technique. *Chem. Eng. Sci.*, **47**, 1079-1089, [https://doi.org/10.1016/0009-2509\(92\)80233-3](https://doi.org/10.1016/0009-2509(92)80233-3).
- Pierson Jr, W. J., M. A. Donelan, and W. H. Hui, 1992: Linear and nonlinear propagation of water wave groups. *J. Geophys. Res.: Oceans*, **97**, 5607-5621, <https://doi.org/10.1029/92jc00115>.
- Prosperetti, A., 1988: Bubble-related ambient noise in the ocean. *J. Acoust. Soc. Am.*, **84**, 1042-1054, <https://doi.org/10.1121/1.396740>.
- Rapp, R. J., and W. K. Melville, 1990: Laboratory measurements of deep-water breaking waves. *Philosophical Transactions of the Royal Society of London. Series A*,

- Mathematical and Physical Sciences*, **331**, 735-800,
<https://doi.org/10.1098/rsta.1990.0098>.
- Rayleigh, L., 1917: On the pressure developed in a liquid during the collapse of a spherical cavity. *London Edinburgh Dublin Philos. Mag. J. Sci. Series 6*, **34**, 94–98,
<https://doi.org/10.1080/14786440808635681>.
- Rogers, W. E., A. V. Babanin, and D. W. Wang, 2012: Observation-consistent input and whitecapping dissipation in a model for wind-generated surface waves: Description and simple calculations. *J. Atmos. Oceanic Technol.*, **29**, 1329-1346,
<https://doi.org/10.1175/jtech-d-11-00092.1>.
- Roshid, M. M., and R. Manasseh, 2020: Extraction of bubble size and number data from an acoustically-excited bubble chain. *J. Acoust. Soc. Am.*, **147**, 921-940,
<https://doi.org/10.1121/10.0000488>.
- Schulz, E. W., 2009: The riding wave removal technique: Recent developments. *J. Atmos. Oceanic Technol.*, **26**, 135-144, <https://doi.org/10.1175/2008jtecho621.1>.
- Tkalich, P., and E. S. Chan, 2002: Breaking wind waves as a source of ambient noise. *J. Acoust. Soc. Am.*, **112**, 456-463, <https://doi.org/10.1121/1.1489436>.
- Weissman, M. A., S. S. Atakturk, and K. B. Katsaros, 1984: Detection of breaking events in a wind-generated wave field. *J. Phys. Oceanogr.*, **14**, 1608-1619,
[https://doi.org/10.1175/1520-0485\(1984\)014<1608:dobeia>2.0.co;2](https://doi.org/10.1175/1520-0485(1984)014<1608:dobeia>2.0.co;2).
- Wilson, J. D., and N. C. Makris, 2008: Quantifying hurricane destructive power, wind speed, and air-sea material exchange with natural undersea sound. *Geophys. Res. Lett.*, **35**,
<https://doi.org/10.1029/2008gl033200>.
- Young, I. R., and L. A. Verhagen, 1996: The growth of fetch limited waves in water of finite depth. Part 1. Total energy and peak frequency. *Coastal Engineering*, **29**, 47-78,
[https://doi.org/10.1016/s0378-3839\(96\)00006-3](https://doi.org/10.1016/s0378-3839(96)00006-3).
- Young, I. R., and A. V. Babanin, 2006: Spectral distribution of energy dissipation of wind-generated waves due to dominant wave breaking. *J. Phys. Oceanogr.*, **36**, 376-394,
<https://doi.org/10.1175/jpo2859.1>.
- Young, I. R., M. L. Banner, M. A. Donelan, C. McCormick, A. V. Babanin, W. K. Melville, and F. Veron, 2005: An integrated system for the study of wind-wave source terms in

finite-depth water. *J. Atmos. Oceanic Technol.*, **22**, 814-831,
<https://doi.org/10.1175/jtech1726.1>.

Zieger, S., A. V. Babanin, W. E. Rogers, and I. R. Young, 2015: Observation-based source terms in the third-generation wave model WAVEWATCH. *Ocean Modell.*, **96**, 2-25,
<https://doi.org/10.1016/j.ocemod.2015.07.014>.